Status of HgCdTe photodiodes at the Military University of Technology

L. KUBIAK, P. MADEJCZYK, J. WENUS, W. GAWRON, K. JÓ WIKOWSKI,
J. RUTKOWSKI, and A. ROGALSKI[*]

Institute of Applied Physics, Military University of Technology,
2 Kaliskiego Str., 00-908 Warsaw, Poland

The paper presents technological achievements in fabrication of cryogenically-cooled and ambient temperature HgCdTe photodiodes carried out during the last four years at the Institute of Applied Physics, Military University of Technology. Because of the complicated and expensive fabrication process, numerical simulation has become a critical tool for the development of HgCdTe bandgap engineering devices. Therefore in the second part of the paper, an original iteration scheme is used to predict the effect of composition and doping profiles on the heterojunction detector parameters.

A novel tipping boat for liquid phase epitaxial (LPE) growth of HgCdTe from Te-rich solutions has been proposed. The successful fabrication of long wavelength infrared (LWIR) $Hg_{1-y}Cd_yTe/Hg_{1-x}Cd_xTe$ heterostructures (y > x) on semi-insulating (111)CdZnTe substrates is presented. The performance of p-on-n double-layer heterojunction (DLHJ) photodiodes at temperature 77 K is analysed.

It is also shown that LPE can be used to realise advanced bandgap engineered multi-junction structures. The parameters and characteristics of the new type of HgCdTe buried photodiodes, operated at near-room temperature (T = 200–300 K) in LWIR spectral range, are reported.

Finally, an effective numerical model for performance predictions of HgCdTe heterostructure device is presented. The model is used to analyse the performance of dual-band HgCdTe photovoltaic detector and mid wavelength infrared (MWIR) HgCdTe heterostructure device. In the last case, it is shown that excess 1/f noise of MWIR non-equilibrium heterostructure device is connected with fluctuation of carrier mobility.

Keywords: liquid epitaxy, HgCdTe photodiodes, multi-junction photodiodes, heterostructure photodiodes, dual-band detectors.

1. Introduction

The Institute of Applied Physics, Military University of Technology, has been active in the field of infrared (IR) photon detectors since the 70s last century. The studies have been concentrated on three main topics:

- technology and properties of HgCdTe photodetectors (photoconductive detectors and photodiodes),
- theory of photoelectrical properties of IR photon detectors, and
- alternative to HgCdTe new ternary alloy systems (such as lead salts, InAsSb, HgZnTe, HgMnTe) and quantum well infrared photodetectors (QWIPs).

The results of these studies are published in many well-known books and monographic papers (book chapters). The most important items are included in Refs. 1–16.

This paper summarizes the results of studies, carried out during the last four years, devoted to technological achievements in fabrication of cryogenically-cooled and ambient temperature HgCdTe photodiodes. Also numerical modelling of fluctuation phenomena in HgCdTe devices is

presented. This numerical model enables us performance prediction of device containing complex heterostructures.

2. Double-layer heterojunction photodiodes

The most commonly used technique for fabricating HgCdTe photodiodes is to make simple n+-on-p homo-junctions by ion implantation into p-type undoped crystals [13]. In 1985, Rogalski and Larkowski [17] indicated that, due to the lower minority-carrier diffusion length (lower mobility of holes) in the n-type region of p+-on-n junctions with thick n-type active region, the diffusion-limited R_0A product of such junctions is larger than for n+-on-p ones. These theoretical predictions were next confirmed by the experimental results obtained for P+-on-n HgCdTe junction (capital letter denotes the wider gap), especially for double layer heterojunction (DLHJ) photodiode. In such a diode, the base n-type layer, deliberately doped with indium at a level of about 10^{15} cm^{-3}, is sandwiched between CdZnTe substrate and wider-gap p-type regions. The p-type layer is doped with arsenic at a level of about 2×10^{17} cm^{-3}. Due to backside illumination (through CdZnTe substrate) and internal electric fields (which are "blocking" for minority

[*]e-mail: rogan@wat.edu.pl
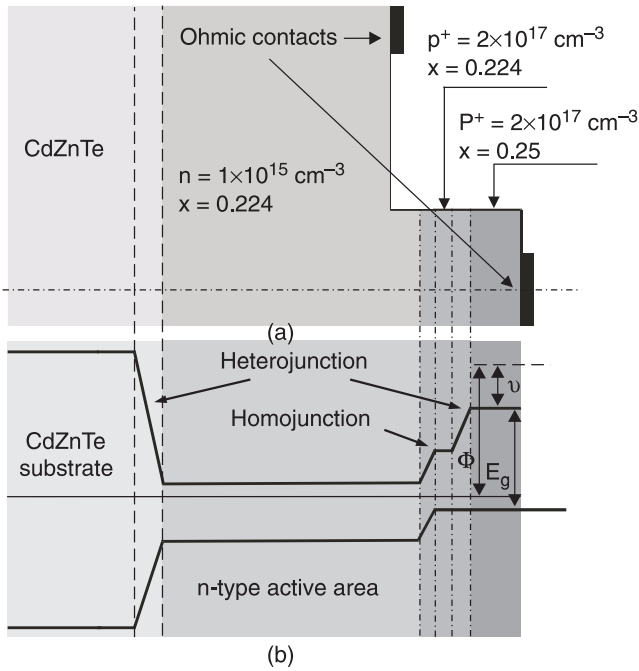
Fig. 1. Double-layer heterojunction HgCdTe photodiode: (a) schematic cross section and (b) band gap energy profile.

carriers), influence of surface recombinations on the photodiode performance is eliminated. Both optical and thermal generations are suppressed in the p-region due to wide gap.

The performance of P+-on-n DLHJ HgCdTe photodiodes at temperature 77 K has been analysed theoretically by Wenus *et al.* [18]. The cylindrical mesa delineated $Hg_{1-x}Cd_xTe$ heterostructure photodiode model is shown in Fig. 1. Material of composition $x = 0.224$ was used as an active base layer of photodiode for detection of long wavelength infrared radiation in the 8–14-μm spectral range.

Estimation of the influence of junction position on photodiode parameters has been carried out by calculation of the R_0A product and quantum efficiency as a function of p-n junction location within the graded region (see Fig. 2). When the junction is located at the side with less x, the R_0A parameter is imperceptibly higher for heterostructure with graded composition. Inside the area with the gradient Δx, the position of p-n junction practically does not influence on photodiode parameters. At the point where junction is located entirely in the wider gap region, R_0A parameter for the abrupt heterostructure is considerably greater. It is caused by the greater potential barrier which efficiently restricts the flow of minority carriers from n-type to p-type region. This barrier also causes a sudden fall of the quantum efficiency. A brief analysis of Fig. 2 makes possible to choose the optimum settlement of the p-n junction within the heterostructure. In the structures with a graded composition, which usually occur in practice (especially using liquid phase epitaxial method), the location of the p-n junction inside the graded region (best in the vicinity of its centre) seems to be the most profitable. Inaccuracies of about 0.5 μm in both directions should not degrade the parameters of the structure in essential degree.

The magnitude of the composition gradient is also very important. It is obvious that the higher Δx gradient induces higher potential barrier, but at a certain range of Δx, the influence on junction parameters is not significant. Figure 3 shows the changes of R_0A and quantum efficiency, η, depending on the gradient of composition for two doping concentrations in p-type cap layer. The acceptable value of the gradient decreases with increase in doping concentration in the cap layer. For typical cap layer doping concentration ($p = 10^{17}$ cm^{-3}) the difference of composition should be about 0.04.
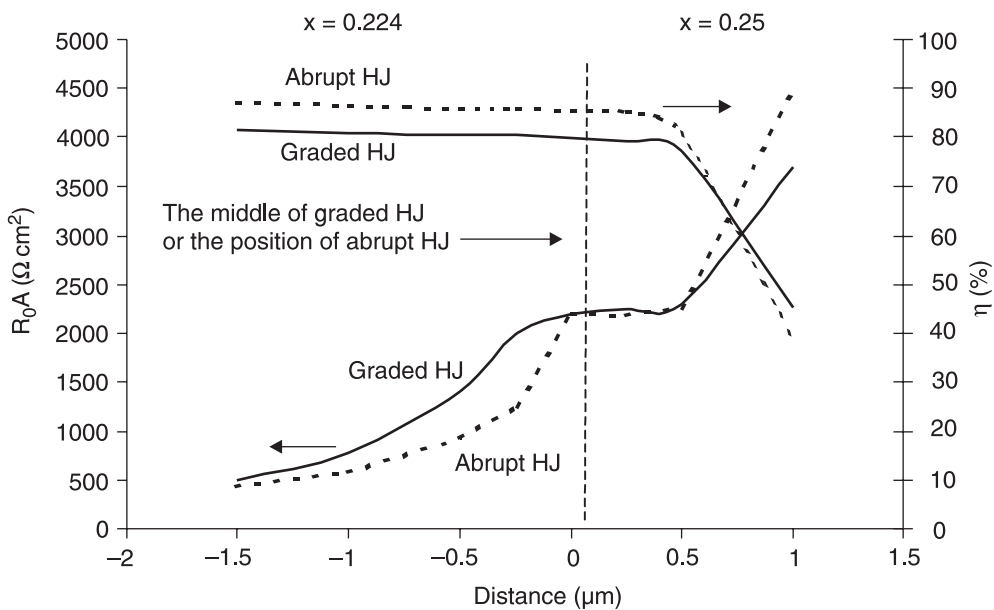
Fig. 2. R_0A product and quantum efficiency versus p-n junction location for graded and abrupt heterojunction.
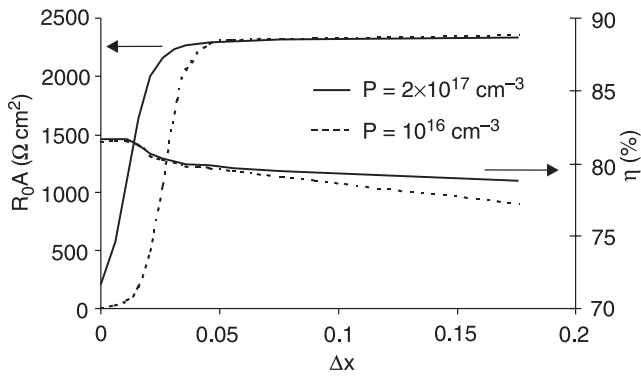
Fig. 3. R_0A product and quantum efficiency versus variation of composition gradient, Δx, for two-cap layer doping concentrations.

2.1. LPE DLHJ growth procedure

Among various epitaxial techniques, the liquid phase epitaxy (LPE) is the most matured method enabling us growth of device-quality homogeneous layers and multi-layered structures [19]. LPE growth must be performed at relatively high growth temperature with adherent interdiffusion and resulting graded interfaces.

The popular method to grow multilayer structures in one *in-situ* process is a slider LPE. Nemirowsky *et al.* [20] have reported on growth of multilayer $Hg_{1-x}Cd_xTe$ with conventional slider systems. However, the results were not quite satisfactory. For growth of $Hg_{1-x}Cd_xTe$ from Te-rich solution using slider technique, the compensation of mercury vapour atmosphere is important in order to obtain good composition control and uniformity of the epilayers. For the first time, double layer heterostructure with satisfactory surface morphology was reported by Chen *et al.* [21] using slider LPE from Te-rich solution at one run. It was possible to form HgCdTe double-layer heterojunction (DLHJ), although the control of growth conditions was quite critical. Tung *et al.* [22] have reported growth of double-layer HgCdTe heterojunction in vertical dipping systems from Hg-rich solution. This approach offers maximum flexibility in junction formation; in utilizing heterojunction formation between the cap layer and absorbing base layer in order to optimise detector performance.

In this paper, we discuss advantage and disadvantage of two types of LPE growth $Hg_{1-x}Cd_xTe$ heterostructures carried out in our laboratory:

*   *in situ* growth of n-type heterolayers in a new graphite boat from Te solution with junction formation by diffusion, and
*   sequential growth of n-type and p-type layers from Te and Hg solutions.

It is shown that a solution charge preparation and LPE growth procedure can help to overcome many of the inherent difficulties: surface defects such as solution droplets, Hg vacancies and unintentional background impurities which control electrical properties, and loss of Hg from

LPE solution, causing changes of composition and liquidus temperature. Next, the performance of P-on-n DLHJ photodiodes operated in the very long wavelength infrared (VLWIR) spectral region at temperature 77 K is analysed.

The long wavelength $Hg_{1-y}Cd_yTe/Hg_{1-x}Cd_xTe$ structures ($y > x$) have been grown on the (111)B CdZnTe (4% Zn) substrate. The CdZnTe substrates, with dimensions of $10\times10\times1$ mm^3, were chemically and mechanically polished and then etched with (2–3)% bromine-methanol solution for a few seconds before loading into the graphite boat. The base active $Hg_{1-x}Cd_xTe$ layers ($0.20 < x < 0.22$) were grown from In doped Te-rich solutions in two types of LPE processes.

The most important part of the first epitaxial growth system is the graphite boat, in which the process takes place. Its construction ensures a contact between the substrate and the two solutions by a dipping method (Fig. 4). The whole boat assembly was acid-cleaned after manufacture and analytical analysis indicated that machined graphite had not contained such impurities as Fe, Cu, Ni, and Na.

Fig. 4. Graphite boat with two source reservoirs.

The tipping LPE system consists of a conventional quartz reactor tube, in which a specially designed ampoule with cone and socket was placed. At the beginning of the process the ampoule was opened, so that the high purity hydrogen could flush the system. Before heating, the ampoule was closed and it remained so throughout the epitaxial process. Such a system design has all advantages of closed systems (it prevents mercury loss) and simultaneously the system may be used repeatedly, because it is very easy to disassemble all its parts.

To obtain a base layer, the homogenisation temperature was 495°C and saturation temperature was 470°C. After completion of homogenisation, the solution was dipped into a separate holder, and was almost completely inserted into reservoir, by turning the quartz ampoule with graphite boat of 90°, thus making contact with the substrate, then practically immersed in the solution. During growth of the first epitaxial layer, the solution temperature decreased at (4–6)°C at a uniform rate 0.1°C/min. After the growth of the first epitaxial layer the system was returned to its initial

position and after a few minutes it was turned to the opposite position (turning of 180°) so that the first epitaxial layer of $Hg_{1-x}Cd_xTe$ on CdZnTe substrate was immersed in the second solution. During growth of the second epitaxial layer of $Hg_{1-y}Cd_yTe$, the solution temperature decreased at (1–2)°C at a uniform rate 0.1°C/min. After the growth process, the whole system was removed from the furnace and cooled to ambient temperature. The scheme of rotation and temperature cycle is shown in Fig. 5.
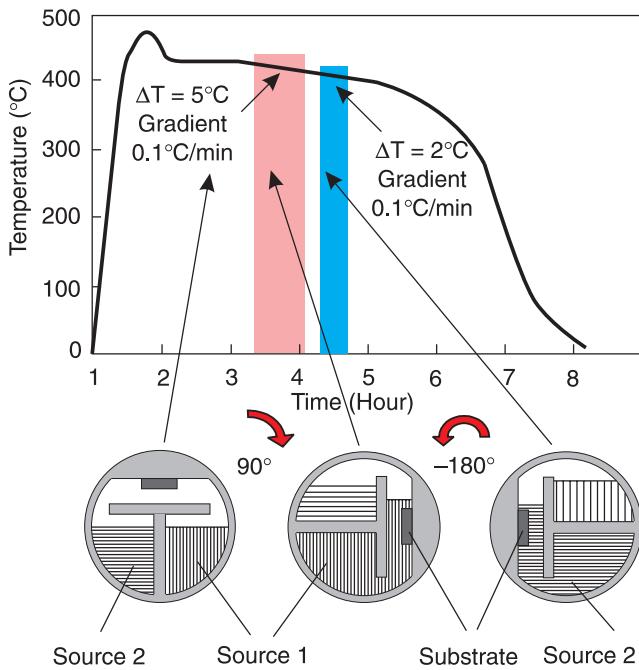
Fig. 5. Temperature cycle during LPE hetero-growth experiment.

The two layers $Hg_{1-y}Cd_yTe$ and $Hg_{1-x}Cd_xTe$ of the heterostructure in the second type of LPE process have been sequentially grown in two separate systems. After growth of the first epitaxial layer from Te-rich solutions the whole system was removed from the furnace and cooled to ambient temperature. To obtain the top cap layer, the heterostructure was loaded to the second graphite boat with Hg-rich solution. LPE growth from an Hg melt, at temperature around 400°C, satisfies cation-rich conditions, although some post growth annealing may be required. The As dopants reside on the Te site to accomplish p-doping. The solution temperature decreased of 10–20°C at a uniform rate 0.1°C/min. After the growth process, the whole system was cooled to 260°C, held at this temperature for 6 hours, removed from the furnace, and cooled to ambient temperature.

In both types of the LPE processes, the heterostructures consist of a thin 1–2-μm wide gap cap layer on n-type 10–15-μm thick HgCdTe epilayer.

p-Type doping during growth (as grown doping) is not possible in first *in-situ* growth method. Usually, after growth the structures are annealed under Hg overpressure. The samples underwent two consecutive annealings; one at

high temperatures (T ≥ 420°C for a short time; e.g., 100 min) and next at 250°C for 24 h immediately after the previous one. The first annealing was performed to diffuse and electrically activate As by substituting As atoms on the Te sublattice, while the second one was to annihilate Hg vacancies formed in the HgCdTe lattice during growth and diffusion of arsenic to restore the sample background to n-type. The concentration of As dopant in p-type cap layer was at a level of about 10^{18} cm^{-3}.

2.2. Characterisation of epitaxial layers

The transport properties of LPE layers were determined from an analysis of Hall effect and resistivity measurements. Optical properties were evaluated using Fourier transform infrared (FTIR) transmission spectra and Nomarski interference contrast photomicrography.
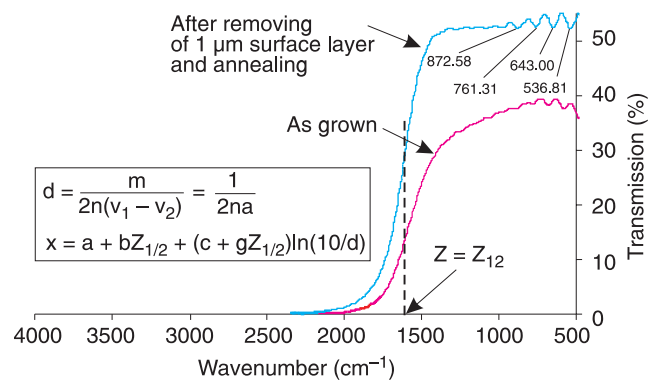
Fig. 6. Transmission spectra for HgCdTe LPE layer.

The FTIR microscopic measurements give both composition and thickness mapping capability over the layer area. An example of typical FTIR data is shown in Fig. 6. The average composition of base sample was $x = 0.221$, with standard deviation of 0.002. It appears that the composition x is more homogeneous than the thickness d of the layer. It can be clearly seen in Fig. 7 which shows uniformity of composition and thickness along the selected axis. There is a small change of thickness at the end of the sample. This effect is connected with the velocity of solder rotation during the
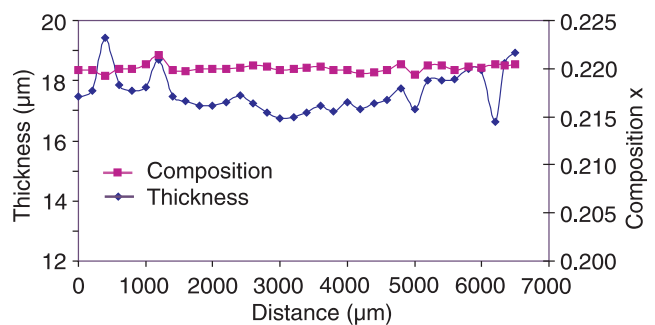
Fig. 7. Uniformity of composition and thickness along the selected axis for the HgCdTe epilayer.
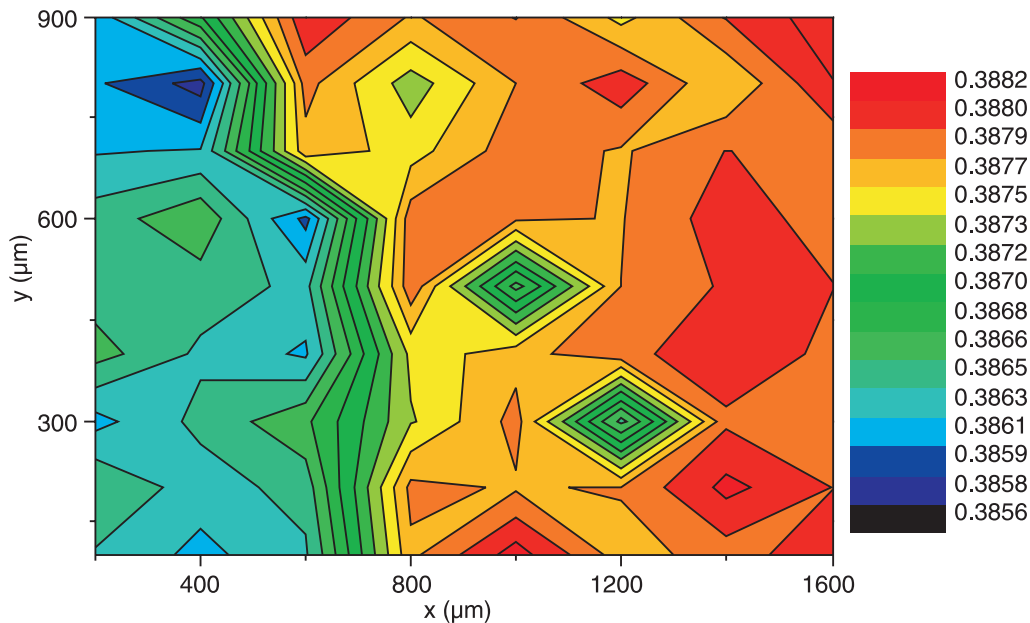
Fig. 8. Composition mapping of HgCdTe sample.

growth of the epilayer. Carefully controlled rotation and programmed cooling improved the spatial uniformity of thickness of the wafers. Uniformity better than 2 μm over 90% of the length of a 17-μm thick epitaxial layer was typical.

Spatial uniformity of the composition for LPE layer is shown in Fig. 8. The mapping was obtained using FTIR spectrophotometer with an *X-Y* stage allowing an automatic mapping of the cutoff wavelength. Figure 8 represents a 0.09×0.16 cm^2 area extracted from a 1×1 cm^2 HgCdTe/CdZnTe sample. For the area compositions variations are reasonable.

The cross-hatch and low density point defects were not observed on a surface of single layers grown on (111) CdZnTe. On the surfaces of two-layer structures, a few small pits appeared due to strain-induced growth; however, significant variations of point defect density were not observed. Surface morphology appeared to be mirror-like to the naked eye, but showed terraced structure under magnification. The terraced structure seems to be extremely difficult to avoid and it is associated with small angular deviation of 0.3° of the substrate surface from a perfect (111) plane. Figure 9 shows a Nomarski interference contrast photomicrograph of an HgCdTe epilayer on (111) CdZnTe substrate.

The composition profiles of classical DLHJ structure analysed by SIMS are shown in Fig. 10. SIMS examination shows a uniform composition beyond a graded region of 3 μm at the layer/substrate interface and 2 μm at the heterointerface. This first grading is consistent with interdiffusion between layer and substrate. The grown double-layer structure consists of an indium doped narrow bandgap active layer and a wider bandgap cap layer. The n-type base HgCdTe layers are typically 15–20-μm thick and thickness of not-intentionally doped cap layers were 2 μm.

SIMS analysis of the HgCdTe layers grown at one growth cycle from Te-rich solution shows that the interdiffusion between cap and base layers is higher then in classical structure, because the temperature of growth of the cap layer is higher and additional temperature cycle connected with diffusion of As dopand is required.

Figure 11 shows the composition change on the cleaved section measured by scanning electron microscope (SEM). Electron microprobe examination of a cross section of epitaxial films shows a uniform composition beyond a 2-μm top layer and CdZnTe substrate.

The electrical properties of the starting HgCdTe wafers were routinely determined by Hall measurements in temperature range between 77 K and 300 K. The measure-
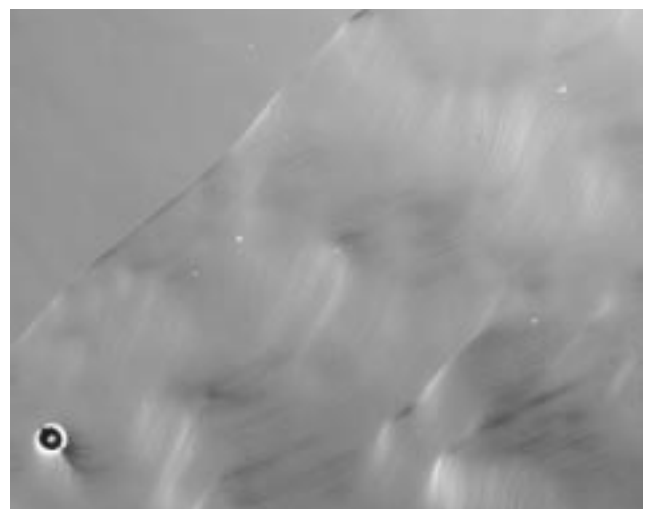
Fig. 9. Surface morphology of HgCdTe LPE layer on (111)CdZnTe substrate.
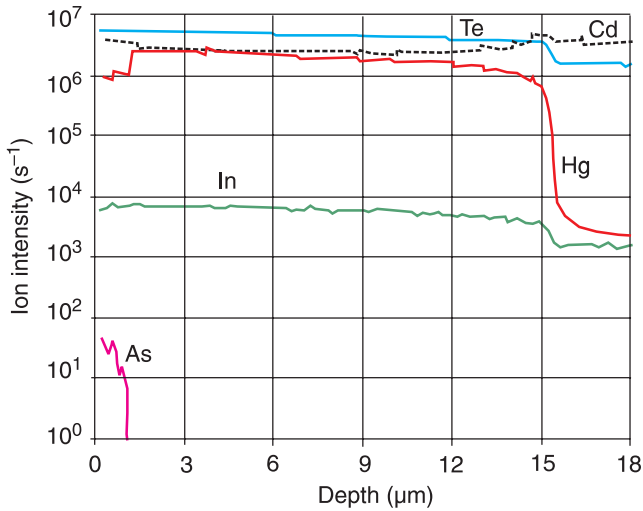
Fig. 10. SIMS composition-depth profiles of 17-μm thick HgCdTe heterostructure on CdZnTe substrate.

ments were carried out on van der Pauw samples fabricated from representative wafers selected from each wafer. Discussions of the Hall effect measurements have become an excellent monitoring for LPE growth with the purity, doping and homogeneity able to be correlated with growth conditions.

As-grown films were p-type with a typical carrier concentration and mobility of 3×10^{17} cm^{-3} and 280 cm^2/Vs, respectively. These films were converted to n-type by post-annealing at 260°C for 24 hours under saturated Hg atmosphere. The In-doped based layers have electron concentration about 3×10^{15} cm^{-3} and mobility 40000 cm^2/Vs. The electrical properties of the cap, wider bandgap energy layer, are difficult to describe. Only SIMS measurements could indicate the As dopant level. The estimated carrier concentration of surface p-type cap layer was in the order of 5×10^{17} cm^{-3}.
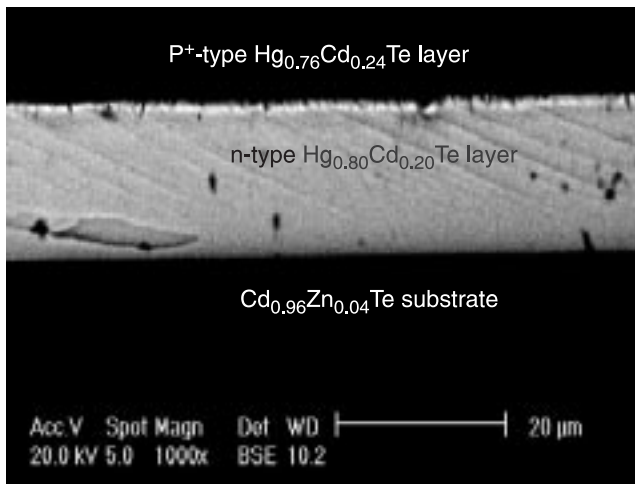
Fig. 11. SEM photo of cross-section of 17-μm thick HgCdTe heterostructure on CdZnTe substrate.

2.3. Properties of DLHJ HgCdTe photodiodes

A mesa-delineated, backside-illuminated HgCdTe photodiode architectures have been applied. Au was used as the ohmic contact for p-type side and In for the n-type side in device fabrication with the junction diameters of 100, 200, and 400 μm. In some cases, the ion milling was applied before In deposition. After p-side contact metallisation, the standard photolithographic techniques and etching in a 5% Br:ethylene glycol were used for the fabrication of mesa structures. Both diodes with CdTe passivation layer as well as without surface passivation layer are analysed. The polycrystalline 0.3 μm-thick CdTe films were deposited using thermal evaporation.

The photodiode performance was established by measurements of the current-voltage (I-V) characteristics, capacity-voltage (C-V) characteristics, and spectral responsivity at 77 K. The photodiodes were mounted in a liquid nitrogen cooled cryostat system and temperature dependences of characteristics were measured in temperature range between 77 K and 300 K. All the I-V and the C-V measurements were done using a computer controlled Keitheley programmable meters. The relative photoresponse spectra were measured with a FTIR spectrometer. The absolute photoresponse was determined using a calibrated blackbody test set, which was composed of a blackbody source, preamplifier, lock-in amplifier, and chopper system. The two essential detector performance parameters influenced on detectivity value, R_0A – the zero bias resistance-area product and quantum efficiency, were analysed.

A typical photodiode I-V characteristic and corresponding dynamic impedance of a 400-μm diameter VLWIR diode at 77 K is shown in Fig. 12. One can easily distinguish two linear regions in the I-V plot. Under forward bias conditions, the resistance of the photodiode is determined by the series resistance, R_s. Two main components contribute to the resistance: the n-type base layer and the electric contacts. In the reverse bias region, however, influence of the shunt resistance, R_{sh}, which is usually similar to the R_{max}-value, predominates. The main source of the shunt re-
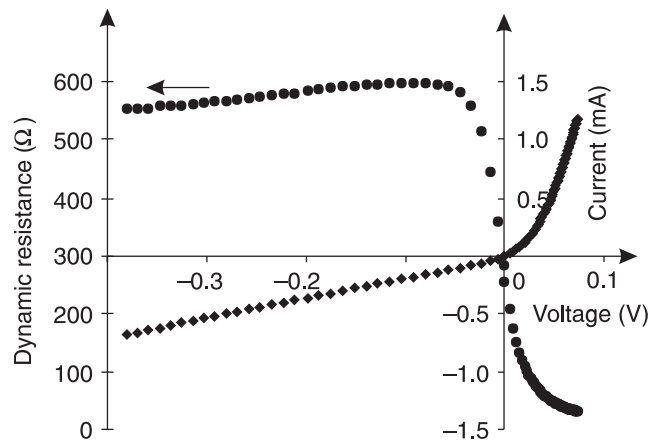
Fig. 12. Current-voltage and dynamic resistance-voltage plots for a DLHJ photodiode.

sistance is a surface leakage current connected with the passivation of the junction. Both the series and the shunt resistances are comparable to the zero-bias junction resistance, R_0.

The shape of I-V curves is also strongly dependent on nominal composition of single crystals. The saturation and shunt currents increase for more long-wavelength photodiodes, and I-V characteristics become more linear. The diodes have theoretical diffusion limited performance down to 100 K but they are limited by surface or tunnelling currents even near zero bias for temperatures 90 K and lower. For very long cutoff wavelengths, interband tunnelling currents could cause a serious problem necessitating development of doping techniques to reproducibly grow/anneal base layers to yield effective doping less than 10^{15} cm^{-3}.

Tunnelling is generally seen for junctions under reverse bias. However, the measured I-V characteristic at high reverse bias voltage has not been determined by tunnelling current. The surface-related current mechanisms, termed surface leakage, with ohmic and breakdown-like behaviour, are probably dominating the reverse current at low temperatures. Thus, the correct passivation is a still major problem.

The modelled and measured quantum efficiencies versus wavelength are displayed in Fig. 13 for photodiodes with the cutoff wavelength λ_c = 14.5 µm at 77 K. The devices have classical spectral response curves. The thickness of photodiode active layer and the value of λ_c are the input parameters to the model. The x value equal to 0.202 is a fitting parameter that the best replicates the shape of the measured quantum efficiency of the detector depending on the wavelength of incident radiation.

The quantum efficiencies of DLHJ photodiodes were bias dependent. At the forward bias, the η-value decreases to zero and then the photocurrent changes its sign and suddenly increases due to domination of photoconduction effect over the photovoltaic signal. It can be clearly seen in Fig. 14, where quantum efficiency is plotted versus bias voltage. At reverse bias voltage quantum efficiency is about 70% and nearly independent of bias. The decrease of
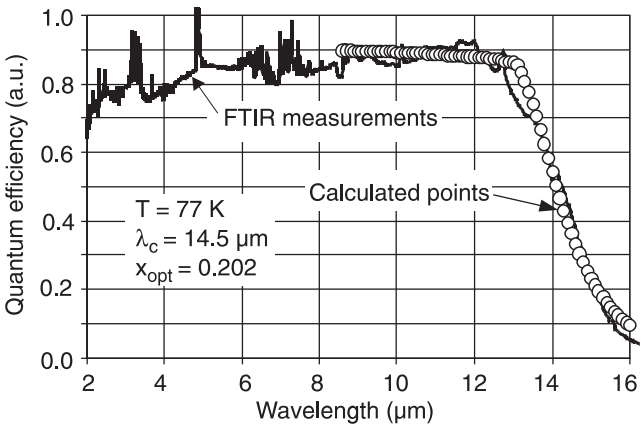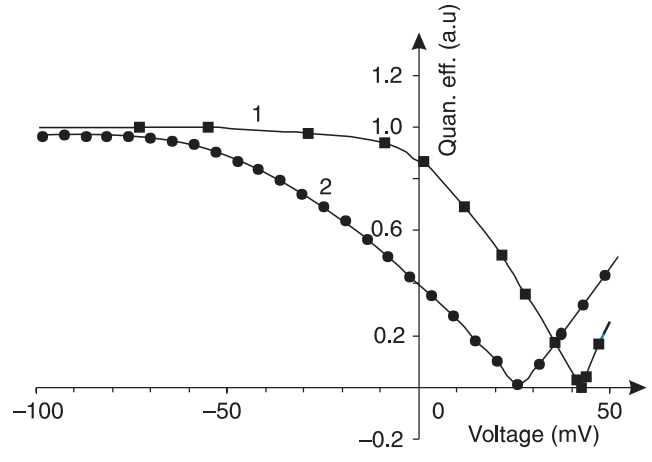
Fig. 14. Normalized quantum efficiency for two photodiodes with different valence-band potential barriers at the heterojunctions (1?2 – increase in the barrier).

η-value at forward bias is connected with valence band barrier formation. The bias dependence of the quantum efficiency for two types of barriers (small – curve 1 and higher – curve 2 in Fig. 14) have been determined. The height of the barrier depends directly on the location of the p-n junction within the heterostructure and it grows when the junction is shifted towards the wider-gap cap region. This effect is more significant in classical DLHJ heterojunction where the junction is placed in higher-gap region. In practice, the control of the junction placement is carried out by a selection of appropriate parameters of annealing (temperature and time) in Hg vapour. The annealing process must be performed carefully to avoid the excessive interdiffusion at the heterojunction.

The noise measurements of photodiodes were made at 77 K in zero background condition, as a function of frequency at a reverse bias voltage of 5 mV. The noise current for these devices was essentially independent of frequency down to 100 Hz. The performance of photodiodes are background limited at temperature 77 K and are gathered in Table 1.

Table 1. LWIR HgCdTe photodiodes operated at 77 K.

Heterojunction	λ_c (µm)	R_0A (Ω cm^2)	η (%)	D^* (cmHz$^{1/2}$W^{-1})
Sequential Te-rich/Hg rich	14.0	2.1	55	2.5×10^{10}
In-situ Te-rich/Hg dif.	12.5	5.3	60	2.8×10^{10}

3. HgCdTe buried multi-junction photodiodes operated near room temperature

Modern epitaxial techniques make possible to grow complex 3-dimensional (3-D) heterostructures with precise control of band gap and doping level profiles which can be applied for high performance optoelectronic devices (see

Fig. 13. Measured and calculated normalized quantum efficiency of a VLWIR photodiode.

e.g. Refs. 13, 23, 24). One example is infrared photo-detector in which the active region can be buried in a wide-gap material, eliminating recombination of photo-generated charge carriers at contacts, surfaces and inter-faces [25]. At the same time parasitic thermal generation of charge carriers can be minimized so, theoretical perfor-mance determined by properties of the absorber region can be achieved in practice. $Hg_{1-x}Cd_xTe$ is an example of vari-able band gap material with almost constant lattice parame-ter. This is one of the reasons for wide application of the material for infrared photodetectors. Piotrowski demon-strated the photodiodes with buried absorber as early as in 1976 [26]. More complex heterostructures can be grown with 3-D band gap engineering using multiple epitaxy, se-lective growth, growth on profiled substrate and combina-tion of the methods [23].

While the performance of conventional LWIR HgCdTe photodiodes operating at near room temperature is very poor due to a low quantum efficiency and a low dynamic resistance, useful performance can be obtained with small-area, multiple junction devices connected in series. The multiple junction devices have additional important advantages [24, 27–29]; the devices have higher resistance because of reduced dark current generation volume in each element, and connection of *n* elements in series results in increased voltage responsivity by the factor *n*. The small thickness of individual elements, below a diffusion length, results in a very short diffusion time what is important for high frequency applications.

In this section, we report an investigation of LPE HgCdTe layers grown on specially prepared CdZnTe (111)B substrates, a new technology of HgCdTe buried multiple photodiodes and preliminary results of measure-ments of spectral response and detectivity of these de-vices.

3.1. Experimental procedure

Lattice-matched CdZnTe single crystals are preferred sub-strates for growth of HgCdTe epilayers with low-dislocat-ion required for high performance devices. $Cd_{0.96}Zn_{0.04}Te$ (111)B oriented substrates supplied by Japan Energy with epi-ready polished surfaces were used for LPE growth. The experimental procedure is based on the idea that epitaxial growth on the top and bottom of mesa is compared with growth on broad, flat surface.
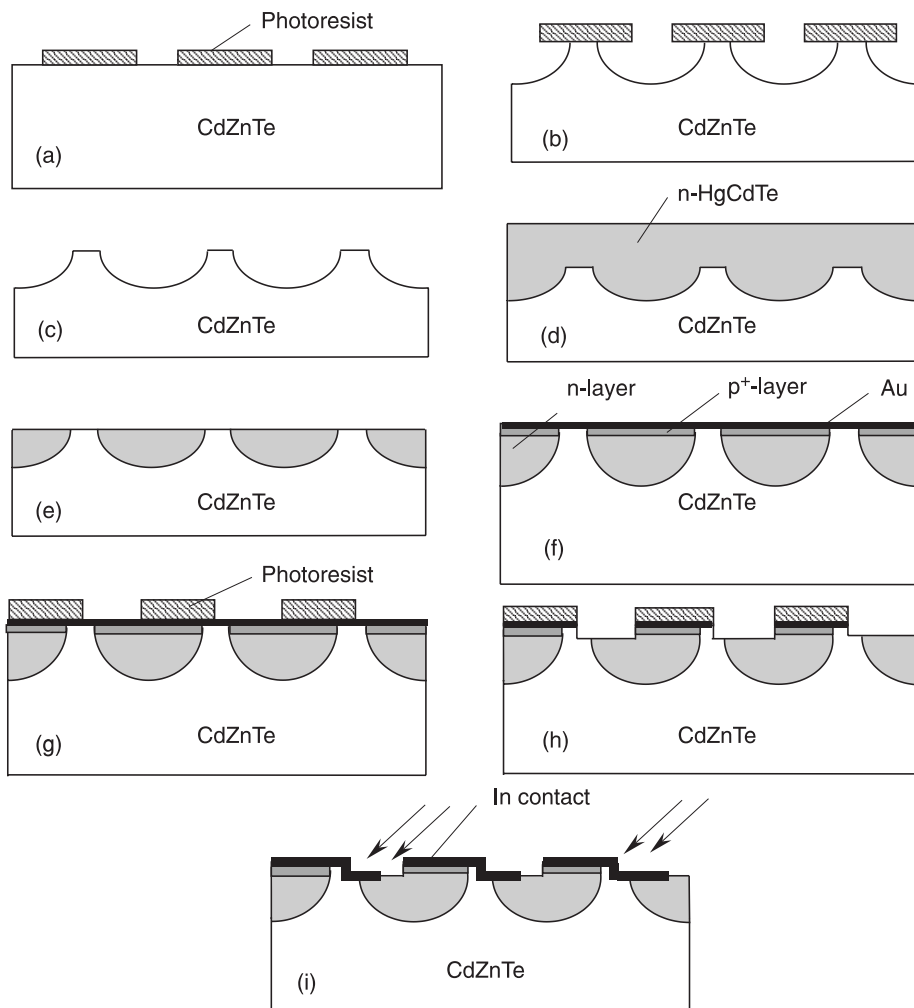
Fig. 15. Typical set of key steps for buried structure and multi-junction photodiode fabrication.

A typical set of key steps for the buried structure and multi-heterojunction photodiode fabrication is shown in Fig. 15. The following steps can be distinguished:

- preparation of CdZnTe substrate for epitaxy:
  (a) deposition of photoresist,
  (b) delineation using chemical etching,
  (c) etching in 3% bromine in methanol solution for several seconds followed by careful cleaning in organic solvents,
- preparation of HgCdTe epitaxial layer:
  (d) deposition of HgCdTe epilayer,
  (e) removing a surface epilayer using chemical etching,
- preparation of multi-junction photodiode:
  (f) formation of p$^+$ region by Sb diffusion and deposition of Au contact,
  (g) deposition of photoresist,
  (h) delineation of multi-structure using chemical etching,
  (i) deposition of In contact.

The wafer was cut into individual multi-junction elements and finally, the individual elements were epoxed to silicon substrate with indium bump contact formation.

LPE from Te melt was selected as the growth method for HgCdTe epilayers. The LPE system and procedure used to growth and characterization of epilayers were presented previously in Section 2.

(a)   (b)
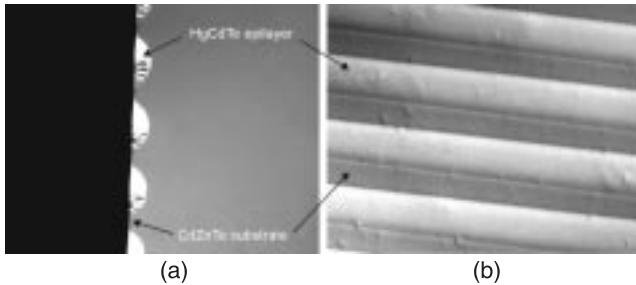
Fig. 16. Cleaved cross section of bars after removed surface epilayer (a) and surface with removed surface epilayer (b). Several buried bars, on 30 μm centres, are visible. The trenches between the bars are broad with a depth of 20 μm.

Figure 16 shows a cleaved cross section of bars after removed surface epilayer and a surface with the removed surface epilayer. Several buried bars, on 30 μm centres, are visible. The trenches between the bars are broad with a depth of 20 μm.

The composition of the epitaxial layers was characterized using FTIR Perkin Elmer microscopy and an X-ray microanalyzator. Figure 17 shows the composition profile along two perpendicular directions (lines *a* and *b*) on cleaved section of the bars after the layer growth. The lines *a* and *b* are marked on SEM view of the bars inside the figures. Variable Hg, Cd, Te profiles across epilayer-substrate interface are typical for LPE technology.
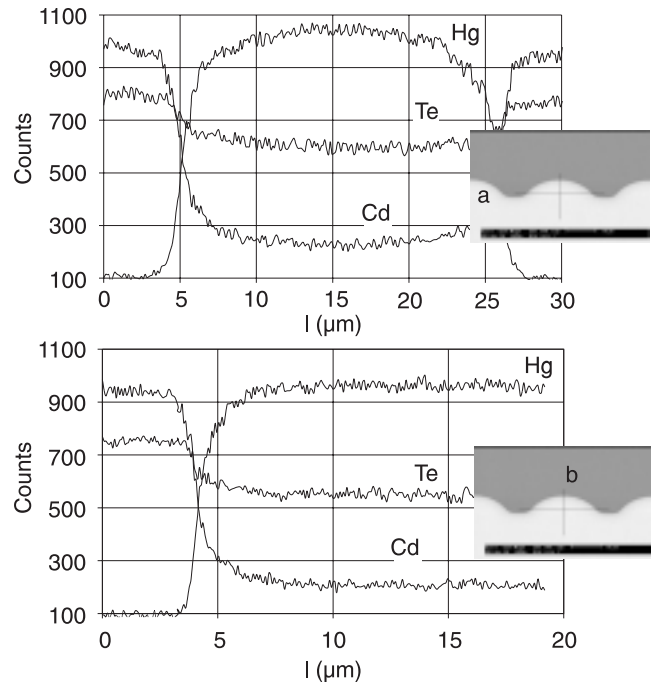
Fig. 17. Composition profiles for Hg, Cd and Te along two perpendicular directions (lines *a* and *b*) on cleaved section of the bars after the growth of LPE Hg$_{1-x}$Cd$_x$Te layers on CdZnTe substrate. The lines *a* and *b* are marked on SEM view of the bars inside the figures. (Philips SEM with X-ray microanalyser EDAX).

Figure 18(a) shows the absorption spectrum in the square area of epitaxial layers marked in Fig. 18(b). The transmission spectra were measured in the range of wave number from 4000 cm^{-1} to 1000 cm^{-1} at a temperature of 300 K using a SPECTRUM 2000 Perkin-Elmer spectrometer with a FTIR microscopy SYSTEM IMAGE. Composition homogeneity along buried epitaxial layers was measured using a FTIR microscopy spectrometer.

3.2. Device characterization

At present, there is no known technology available to fabricate the required Hg$_{1-x}$Cd$_x$Te structures with both closely spaced (a few microns) and deep ($\approx$10 μm) heterojunctions. Future technologies based on selective area epitaxy, epitaxial re-growth, and ion beam processing may offer the means for optimised multi-heterojunction detectors. The device implementation presented in this paper represents a near optimal solution based on relatively simple, quasi-equilibrium growth LPE technique. The performed multi-heterojunction device consists of a structure based on backside-illuminated photodiodes. The epitaxial layers exhibited near uniform composition in the uppermost 4/5 of the total thickness, while a significant grading occurred in the lower portion of the layer (1/5 of total thickness), with the bandgap increasing toward the substrate.

n-type absorbing regions of multi-junction photodiodes were fabricated during LPE process using deliberately doped melt with indium at a level of about 10^{15} cm^{-3}. p-n

(a)

(b)
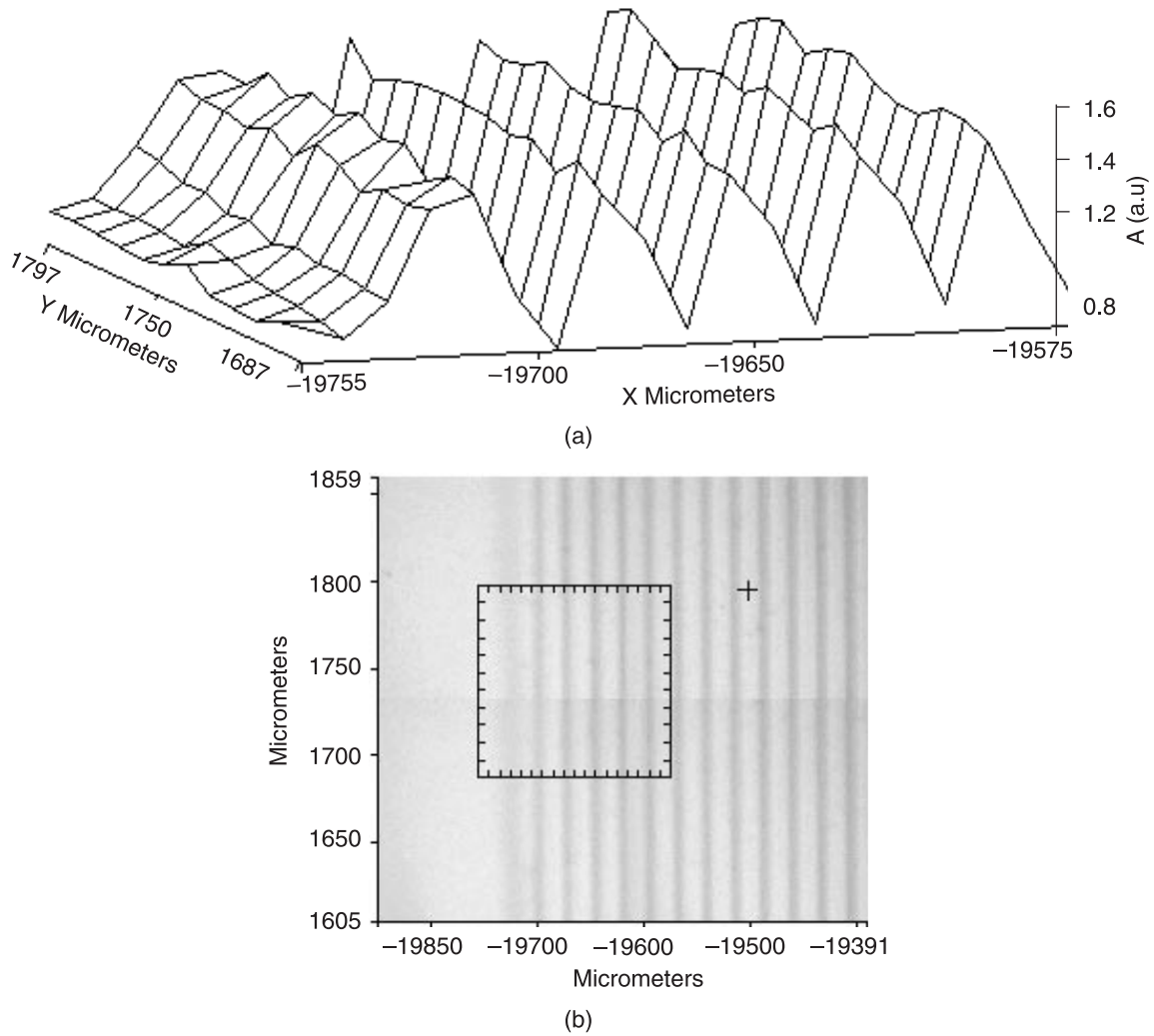
Fig. 18. Absorption spectrum (a) in the square area [marked in figure (b)] of HgCdTe epitaxial layers buried in CdZnTe substrates.

junctions were formed by diffusion using Sb as the dopant at a level of about 10^{18} cm^{-3}. To active Sb as acceptor, it must occupy a Te site in the lattice. Full Sb activation and annihilation of Hg vacancies were achieved during post growth annealing. Indium was used as an electrical contact to n-type active regions.

Devices with one square millimetres buried multi-junction areas have been fabricated and characterized. Both spectral voltage responsivity and resistivity measurements were carried out. Figure 19 shows the spectral voltage responsivity of experimental 33 single p-n buried junction connected in series (total area $w \times l$ with w = 1 mm and l = 1 mm; $p \approx 10^{18}$ cm^{-3}, $n \approx 10^{15}$ m^{-3}). It was found, that the voltage responsivity is strongly dependent on the operation temperature. Cooling with two-stage Peltier cooler causes increase in the peak spectral response by approximately one order of magnitude. Moreover, enhancement of responsivity is stronger at the long wavelength tail of responsivity curve. Higher responsivity at lower temperature in short wavelength range is due to the increased junction resistance, while in the long wave-

length spectral range an improvement in quantum efficiency is more decisive.

The experimental data and theoretically predicted parameters (voltage responsivity and detectivity) of
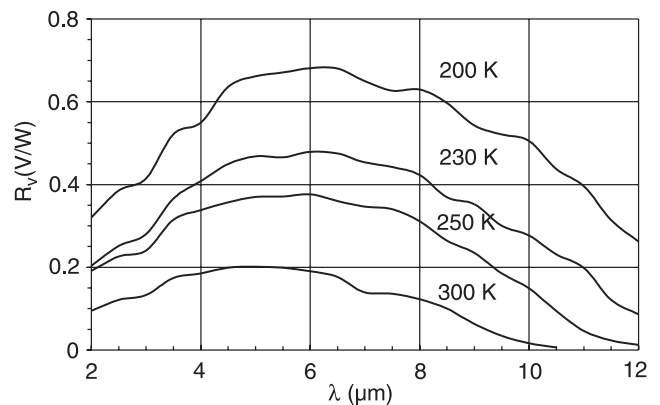
Fig. 19. Spectral voltage responsivity of 33 single p-n buried junction connected in series (total area w = 1 mm, l = 1 mm, $p \approx 10^{18}$ cm^{-3}, $n \approx 1 \times 10^{15}$ cm^{-3}) at different temperatures.

Table 2. Performance of $Hg_{0.82}Cd_{0.18}Te$ buried multi-junction photodiode.

Temperature (K)	300	250	230	200
Resistance (Ω)	12.5	17.5	21	31.5
Experimental voltage responsivity (mV/W)	200	380	480	680
Theoretical voltage responsivity (mV/W) (single-junction device, A = 1×1 mm^2)	36	68	92	156
Detectivity-experiment (cmHz$^{1/2}$/W)	4.3×10^7	7.7×10^7	9.3×10^7	1.1×10^8
Detectivity-theory (cmHz$^{1/2}$/W)	2.1×10^8	3.5×10^8	4.5×10^8	7×10^8

$Hg_{1-x}Cd_xTe$ ($x = 0.18$) buried multi-junction photodiode are gathered in Table 2. We can notice several times increase in voltage responsivity of multiple-junction device in comparison with theoretically predicted value for single-junction device with the same active area (1×1 mm^2). However, discrepancy exists between experimental data and theoretical upper limit of detectivity.

4. Numerical modelling of HgCdTe heterostructure device's performance

Because of the complicated and expensive fabrication process, numerical simulation has become a critical tool for the development of HgCdTe bandgap engineering devices. Some numerical methods for modelling of photoelectrical phenomena in devices were developed [30–36], but they were limited to simple models. For structures with strong inhomogeneities in the energy band gap and doping, simplifying assumptions does not, however, apply. In the regions of strong inhomogeneities, nonequilibrium effects occur, strongly influencing the basic physical parameters, such as carrier lifetime, carrier concentration, absorption coefficient, etc. These parameters vary significantly with the bias voltage, temperature, and illumination of the structure. All these effects have to be taken into account in the theoretical analysis.

4.1. Numerical method

The photoelectrical phenomena in any type of semiconductor device can be analysed using forward-condition steady-state analysis [33]. Basic equations for d.c. analysis have the well-known equations: continuity equations for electrons and holes and Poisson's equation, which are collectively referred to as the Van Roosbroeck model [37]

$$\frac{\delta n}{\delta t} = \frac{1}{q} div \vec{j}_e + (G - R)_e = 0$$

continuity equation for electrons, (1)

$$\frac{\delta p}{\delta t} = \frac{1}{q} div \vec{j}_h + (G - R)_h = 0$$

continuity equation for holes, (2)

$$\Delta^2 \psi = -\frac{q}{\varepsilon_o \varepsilon_r}(N_d - N_a + p - n) - \frac{1}{\varepsilon_r}\nabla\psi\nabla\varepsilon_r$$

Poisson's equation, (3)

where n and p are the hole and electron concentrations, j_e and j_h are the electron and hole current densities, q is the electron charge, Ψ is the electrostatic potential, N_d is the concentration of donors, N_a is the concentration of acceptors, and $\varepsilon_o\varepsilon_r$ is the permittivity of the semiconductors. G and R denote the carrier generation and recombination rates, respectively.

The current density can be expressed as a sum of diffusion and drift components

$$\vec{j}_e = qD_e\vec{\nabla}n - q\mu_e n\vec{\nabla}\psi,$$ (4)

$$\vec{j}_h = -qD_h\vec{\nabla}p - q\mu_h p\vec{\nabla}\psi,$$ (5)

where μ_e and μ_h are the electron and hole concentrations, D_e and D_h are the electron and hole diffusion coefficient.

Equations (4) and (5) can be expressed simpler as a function of the Fermi quasi-level Φ_e and Φ_h

$$\vec{j}_e = q\mu_e n\vec{\nabla}\Phi_e,$$ (6)

$$\vec{j}_h = q\mu_h p\vec{\nabla}\Phi_h.$$ (7)

The main problem with solving of equations (1)–(5) is related to their non-linearity. The carrier concentrations of electrons and holes, the concentrations of ionised impurities, and generation-recombination term (G–R), are rather complicated due to non-linearity of the electrostatic potential Ψ and the Fermi quasi-level Φ. To solve Eqs. (1), (2), and (3) taking into account relations (6) and (7), it is necessary to linearize Eqs. (1)–(3), (6), and (7), and then to calculate Φ_e and $\Phi_{h.}$. The numerical procedure is described in Ref. 38. In practice, the calculations are started by solving the Poisson's equation assuming thermodynamic equilibrium. This leads to constant Fermi levels across the structure what is then used as the reference energy for further calculations. At the next step, the spatial distribution of

electrostatic potential, concentrations of electrons, holes, ionised impurities, and electron affinity, are calculated iteratively. For the calculation the non-parabolicity and degeneration are taken into account. Neumann boundary conditions have been used for calculations of electrical potential at equilibrium conditions. The calculated electrostatic potential at the equilibrium is used then to solve equations (1)–(3) for the non-equilibrium case taking the equilibrium solutions as the initial solutions in the iterative procedure. The electrical bias has been taken into account by the change of the boundary conditions at contact regions. To calculate the influence of illumination, the optical generation rate to the thermal generation rate are added. The concentrations and generation-recombination rates in Eqs. (1)–(3) are expressed as the functions of potential and Fermi quasi-levels without any simplified assumptions. The linearization of the iterative equations has been achieved by gradual change of electric bias and optical power density.

Below, two examples of application of the numerical modelling for performance predictions of HgCdTe heterostructure device are presented: for dual-band HgCdTe photovoltaic detector [39] and for mid-wave infrared (MWIR) HgCdTe heterostructure device [40].

4.2. Dual-band HgCdTe photovoltaic detector performance

Reine and co-workers [41] have proposed a novel simultaneous middle wavelength infrared/long wavelength infrared (MWIR/LWIR) dual-band HgCdTe detector fabricated from four-layer P-n-N-P structures (the capital letters mean the materials with larger bandgap energy) grown *in situ* by the interdiffused multilayer process MOCVD onto lattice-matched CdZnTe substrates. The LW photodiode is a P-on-n heterojunction grown directly on the top of the MW photodiode, which is an n-on-P heterojunction. A thin n-type compositional barrier layer between the MW and LW absorber layers forms isotype n-N heterojunction at the interface which prevents MW photocarriers from diffusing into the LW absorber layer.

Simplified geometry of a device structure, composition and doping concentration profiles of the four-layer P-n-N-P MW/LW dual-band HgCdTe detector like those described by Reine *et al.* are shown in Fig. 20. Profiles of alloy composition and doping concentrations (donors and acceptors) are similar to SIMS depth profile data taken on a representative P-n-N-P detector structure [41].

The assumed composition and doping concentration profiles permit us to calculate the spatial distribution of electrostatic potential and band structure of a device. Figure 21 presents the spatial distribution of electrostatic potential along AB line as shown in Fig. 20(a). We can see that the potential barrier at a depth about 10 µm blocks the flow of holes (the minority carriers) from LW to MW region. This inference is also supported by the spatial distri-
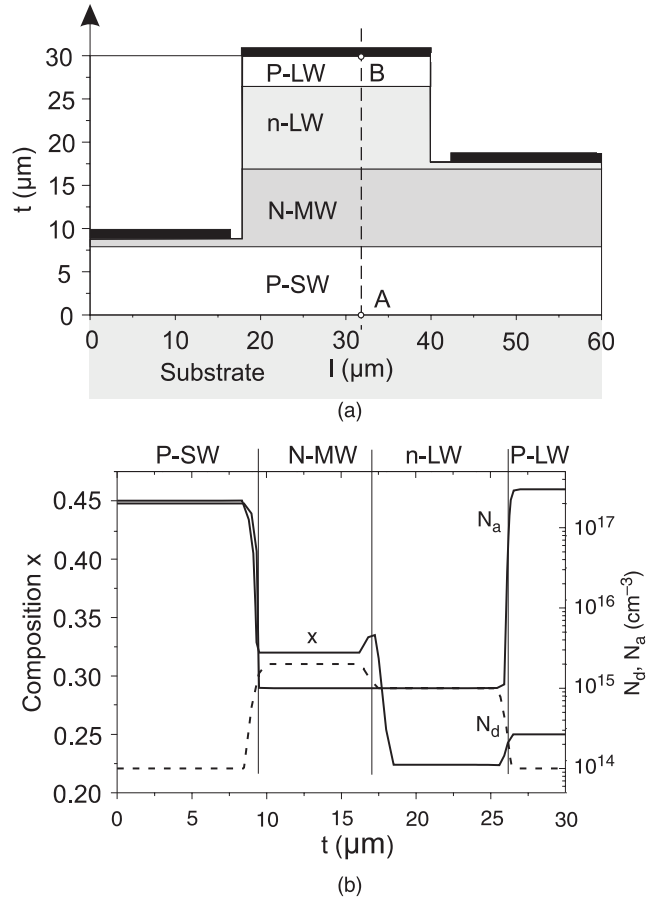
Fig. 20. P-n-N-P dual band HgCdTe detector: (a) cross-section of the device, (b) composition and doping profiles along AB line shown in figure (a).

bution of the bandgap structure shown in Fig. 22. This figure demonstrates that the energy barrier in the valence band together with N-n isotype heterojunction can effectively block the flow of holes generated optically in the n-type base region of LW photodiode. On the other hand, a small
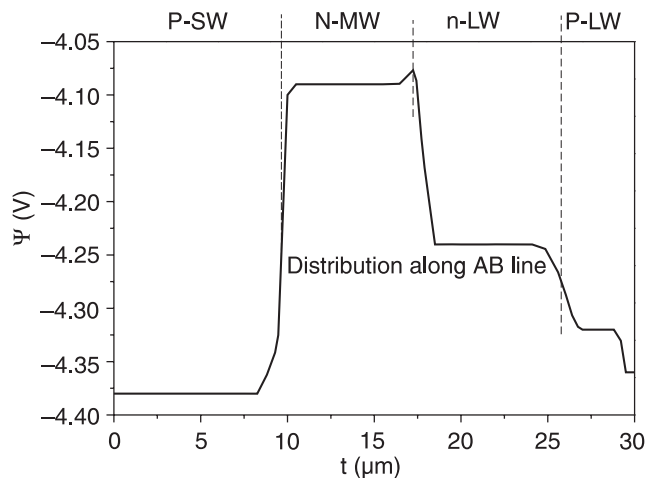
Fig. 21. Spatial distribution of electrostatic potential along AB line as shown in Fig. 20(a).
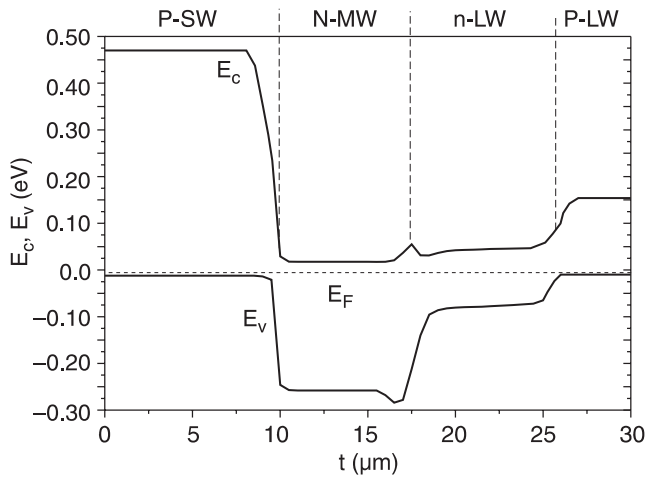
Fig. 22. Energy bandgap of P-n-N-P HgCdTe structure.

barrier of N-n heterojunction does not effectively block the flow of optically generated holes in the n-type MW photodiode to the n-type base region of LW photodiode. As a result, considerable MW-to-LW crosstalk can be observed. This is unfavourable effect disturbing operation of the LW photodiode.

Figure 23 shows the measured and theoretically predicted relative spectral responses for MW and LW detectors in one dual-band detector. The MW and LW average cutoff wavelengths at 77 K are 4.3 μm and 10.1 μm, respectively. The MW response is quite small for wavelengths beyond 4.5 μm, indicating low LW-to-MW crosstalk consistent with the measured crosstalk value of 0.4%. The measured MW response at the wavelength less than 2.9 μm is suppressed, presumably due to a high recombination rate for SW photocarriers at the interface between the wide-gap p-type window layer and the CdZnTe substrate (see Fig. 20). The expected filtering of the LW photodiode re-

sponse spectrum by the MW layer is clearly evident in the sharp increase in LW response at 4.0 μm. According to Ref. 41, some extraneous features in the LW spectrum of 6–7 μm are due to water vapour absorption.

4.3. MWIR HgCdTe heterostructure device performance

It is known that the $1/f$ noise may result in the fluctuations of the carrier mobility. It is not clear, however, why strong $1/f$ noise is observed in reverse-biased HgCdTe non-equilibrium photodiodes, when saturation currents are usually very low. In the present section we try to answer on this question. The key to theoretical analysis of noise phenomena in semiconductor devices seems to be the set of "transport equations for fluctuations" (TEFF), which were developed and solved by Józwikowski et al. in Refs. 38 and 40. The calculations allow one to examine the influence of different noise sources on noise currents that occur in electronic systems in which semiconductors are embedded.

Let us consider a p^+-p^--π-n^--n^+ five layer cylindrical structure (with the diameter of 35 μm) like those described by Elliott et al. [42]. Simplified geometry of the device structure, composition and doping concentration profiles are shown in Fig. 24. Profiles of the alloy composition and doping concentration (donors and acceptors) are similar to the measured SIMS depth profiles.

Figure 25 presents the spatial distribution of the band structure of the device along line AB [see Fig. 24(a)]. The calculations were carried out for a non-cooled device in equilibrium (solid lines) and a reverse-biased one with $U = 0.1$ V. The calculated saturation current is approximately 900 nA and is thus higher than that obtained by Elliott et al. (640 nA). The difference is probably due to the effects of the contact (we assumed ideal ohmic contacts in our considerations).
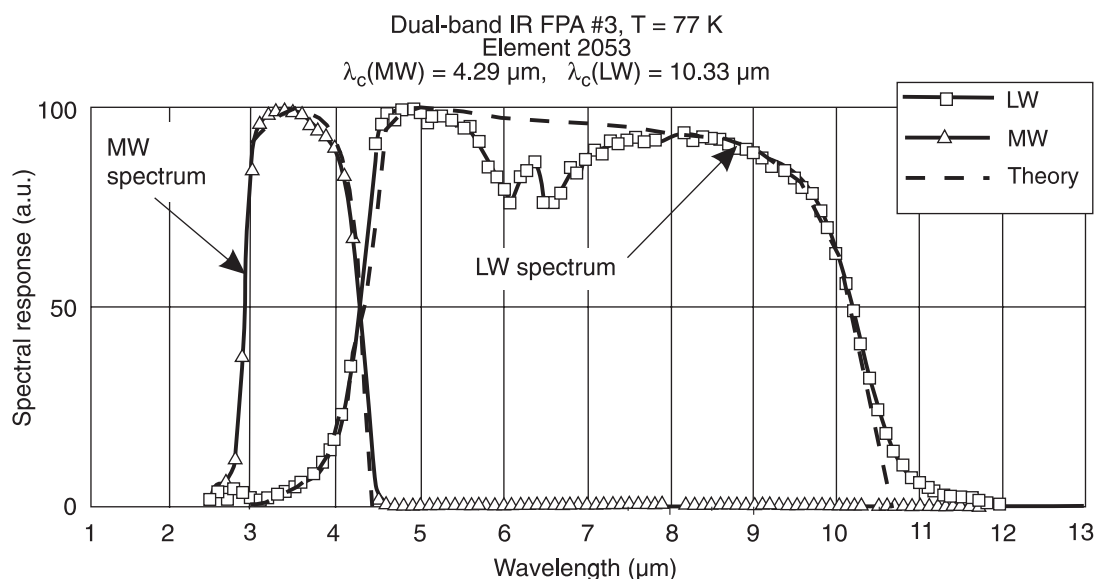
Fig. 23. Comparison of experimentally measured and calculated relative spectral responses for dual-band MW/LW HgCdTe detector.
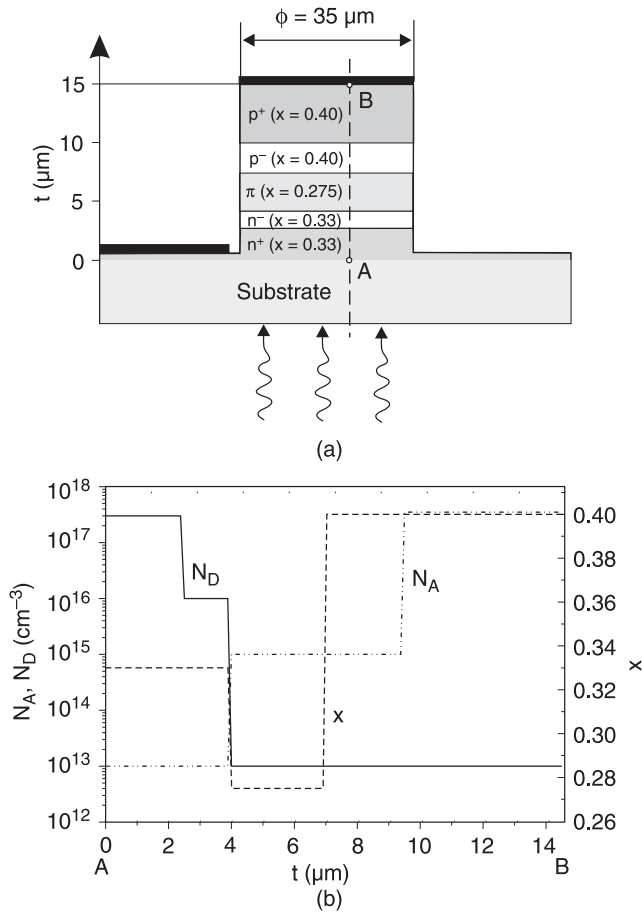
Fig. 24. The cross-section of the investigated structure (a), doping and mole-fraction profile (b).

The electric fields created in the device under reverse bias strongly affect carrier concentration. It can be seen in Fig. 26, where the spatial distribution of electron and hole concentrations along line AB is presented in equilibrium and in conditions of the reverse bias of 0.1 V. Both electrons and holes in the central narrow gap region are ex-
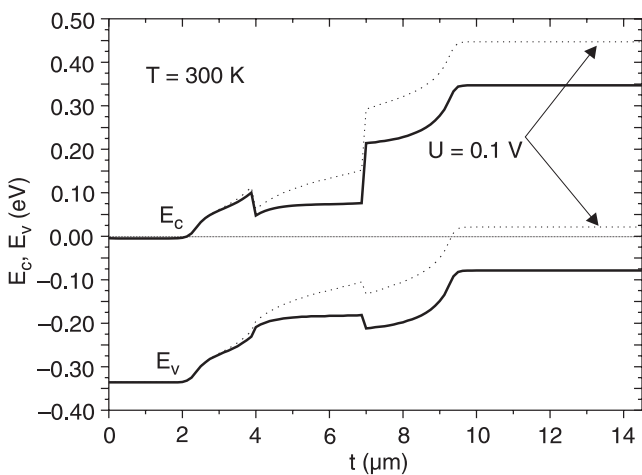
Fig. 25. The energy bandgap of p⁺-p⁻-π-n⁻-n⁺ HgCdTe structure at zero bias (solid lines) and at 0.1 V reverse bias (dotted lines).
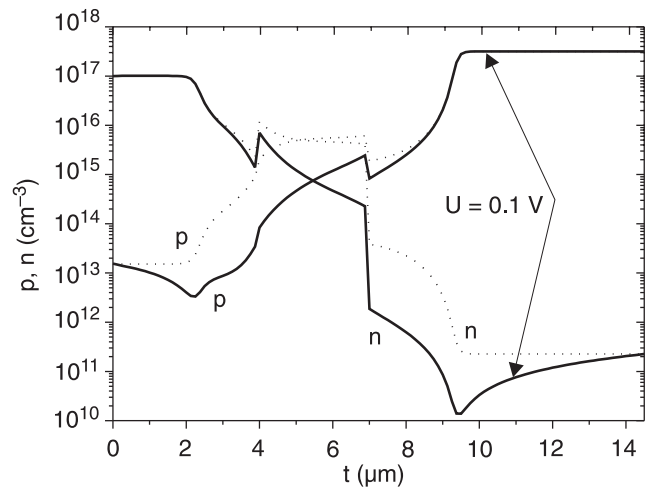
Fig. 26. The spatial distribution of doping profile at zero bias (dotted lines) and at 0.1 V reverse bias (solid lines).

tracted by the electric field caused by the reverse bias $U = 0.1$ V (solid lines). In heavily doped regions with wider gaps a considerable decrease in minority carrier concentrations is observed. Decreasing minority carrier concentrations leads to decreasing thermal generation rates of the Auger band-to-band processes. This seems to be the best way to increase the detectivity of the device since the thermal g-r noise is decreased. Unfortunately, the decrease in the carrier concentrations leads to increased band carrier mobility and its fluctuations hence increasing the low-frequency noise [38,43]. As a consequence a decrease in detectivity is observed in non-equilibrium devices operating under a reverse bias.

Figure 27 shows the calculated spectral intensity of noise current in reverse biased ($U = 0.1$ V) heterostructures at selected temperatures. The experimental data (solid lines
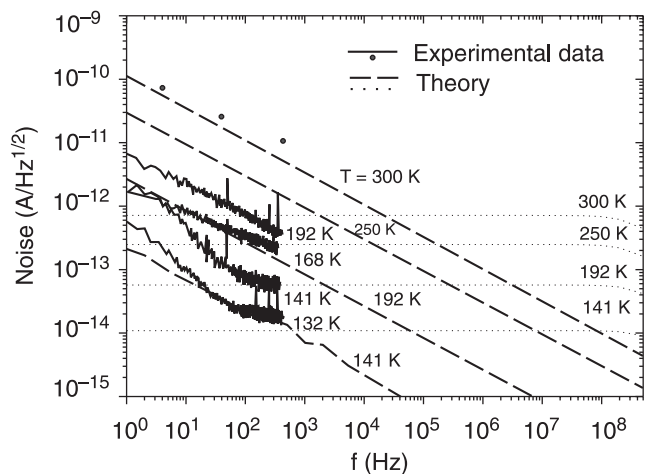
Fig. 27. Spectral intensity of noise current in reverse biased ($U = 0.1$ V) heterostructures for selected temperatures. The experimental data (solid lines and points) are taken after Elliott *et al.* [42]. The dashed lines denote situation when only fluctuations in band carrier were considered as random noise sources in TEFF.

and dots) are taken after Elliott *at al.* [42]. The dashed lines correspond to the situation where only the fluctuations in band carrier mobility were considered as random noise sources in TEFF. The 1/*f* frequency dependence of this noise is observed. Dotted lines represent the situation where only the fluctuations in g-r rates are considered as a random noise source in TEFF. The g-r noise is independent of frequency at all considered temperatures up to the frequency of 10^8 Hz. In all considered temperatures 1/*f* noise prevails for low frequencies, but the 1/*f* knee is shifting to lower frequencies when the device is cooled. Rather good agreement between the simulation and experimental results is obtained near the room temperature. The discrepancies, especially at lower temperatures (below 200 K), may be due to the fact that the applied model is limited to only two scattering processes and does not consider the effect of misfit dislocations and contacts in heterostructures. We did not consider the effect of high electric field on carrier mobility and its fluctuations, either.

Figure 28 explains the reason why high 1/*f* noise is observed in the considered heterostructures. The solid lines represent spatial distributions of the electric field and the distribution of spectral intensity of noise power densities (for 100 Hz of frequency) along line AB in a non-cooled, reverse-biased ($U = 0.1$V) device. The noise power density was examined using only mobility fluctuations (curve marked as 1/*f*) as a random noise source and then using only the fluctuations of the rate of g-r processes (curve marked as g-r). The overall effect is the algebraic sum of the effect of the two sources because TEEF are linear. We may observe a strong correlation between the distribution of noise power density and that of electric field. The noise is mainly generated in the junction regions where the electric field is the highest. The 1/*f* noise is mainly generated in the p^+-p junction. The g-r noise is, on the other hand, strongly reduced due to the extraction effect. In ohmic contact regions the noise generation vanishes, because no fluctuations are assumed here.
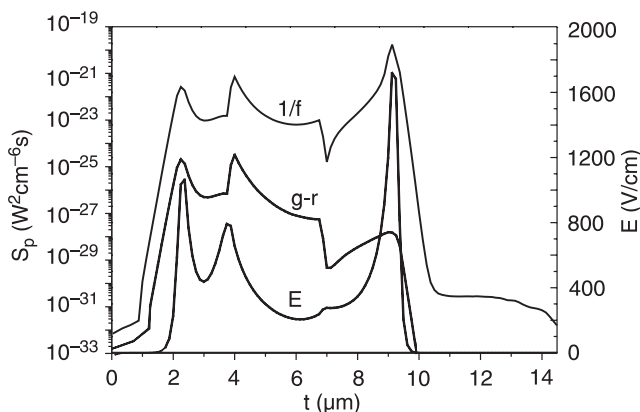
Fig. 28. Spatial distribution along line AB of the electric field (E curve) and the noise power densities (1/*f* and g-r curves) under 0.1 V reverse biased in non-cooled device.

5. Conclusions

The paper presents considerable technological progress in fabrication of cryogenically-cooled and ambient temperature HgCdTe photodiodes carried out at the Institute of Applied Physics (IAP), Military University of Technology during the last four years.

Two types of tipping liquid phase epitaxy (LPE) processes were used to grow HgCdTe double layer heterojunction photodiodes: classical (base layer grown from Te-rich solution and top layer – from Hg-rich solution), and *in-situ* grown (two layers from Te-rich solution with As diffusion to p-on-n junction formation). The semi-closed system with a tipping graphite boat enables us reproducible production of heteroepitaxial layers suitable for fabrication of good quality LWIR photodiodes.

The paper also presents technology and performance of a new type of buried multi-junction HgCdTe LWIR photodiodes operated at near room temperature. The spectral response and detectivity measurements indicate that the potential device performance limit has not been achieved, yet. However, the results are promising and it is expected to improve the devices performance using better processing techniques.

Finally, an effective numerical model for performance predictions of HgCdTe heterostructure device is presented. To demonstrate usefulness of the model, the effect of composition and doping profiles on the detector parameters is presented. Both dual-band photovoltaic detector and MWIR heterostructure device are considered. It is shown that excess 1/*f* noise of MWIR non-equilibrium heterostructure device is connected with the fluctuation of carrier mobility.

The LPE is the most matured method among the various HgCdTe epitaxial techniques. However, LPE technology is limited for a variety of advanced heterostructure devices. LPE typically melts off a thin layer of the underlying material and each time an additional layer is grown as a result of relatively high growth temperature. Additionally, the gradient in x-value in the base layer of p-on-n junction can generate a barrier transport in certain cases due to interdiffusion. These limitations have provided an opportunity for vapour phase epitaxy; MBE and MOCVD. Further improvement in fabrication of HgCdTe heterojunction devices at the IAP will be possible owing to installation of MOCVD equipment.

References

1. J. Piotrowski and A. Rogalski, *Semiconductor Infrared Detectors*, WNT, Warsaw, 1984. (in Polish).
2. A. Rogalski and J. Piotrowski, "Intrinsic infrared detectors", *Progress in Quantum Electronics* **12**, 87–289 (1988).
3. A. Rogalski, "InAs$_{1-x}$Sb$_x$ infrared detectors", *Progress in Quantum Electronics* **13**, 191–231 (1989).
4. A. Rogalski, "Hg$_{1-x}$Zn$_x$Te as a potential infrared detector material", *Progress in Quantum Electronics* **13**, 299–353 (1989).

5. A. Rogalski, "Hg$_{1-x}$Mn$_x$Te as a new material for infrared detectors", *Infrared Physics* **31**, 117–166 (1991).

6. A. Rogalski (editor) *Selected Papers on Semiconductor Infrared Detectors*, SPIE Milestone Series, Vol. MS 66, SPIE Optical Engineering Press, Bellingham, USA, 1992.

7. F.F. Sizov and A. Rogalski, "Semiconductor superlattices and quantum wells for infrared optoelectronics", *Progress in Quantum Electronics* **17**, 93–164 (1993).

8. A. Rogalski, *New Ternary Alloy Systems for Infrared Detectors*, SPIE Optical Engineering Press, Bellingham, 1994.

9. A. Rogalski, *Infrared Photon Detectors*, SPIE Optical Engineering Press, Bellingham, 1995.

10. J. Piotrowski and A. Rogalski, "Photoelectromagnetic, magnetoconcentration and Dember infrared detectors" in *Narrow-Gap II–VI Compounds and Electromagnetic Applications,* pp. 506–525, edited by P. Capper, Chapman & Hall, London 1997.

11. A. Rogalski, *Infrared Detectors,* Gordon and Breach Science Publishers, Amsterdam, 2000.

12. A. Rogalski, "Hg-based alternatives to MCT," in *Infrared Detectors and Emitters: Materials and Devices*, pp. 377–400, edited by P. Capper and C.T. Elliott, Kluwer Academic Publishers, Boston, 2001.

13. A. Rogalski, K. Adamiec, and J. Rutkowski, *Narrow-Gap Semiconductor Photodiodes*, SPIE Press, Bellingham, 2000.

14. Z. Bielecki and A. Rogalski, *Detection of Light*, WNT, Warsaw, 2001 (in Polish).

15. A. Rogalski, "Comparison of photon and thermal detectors performance", in *Handbook of Infrared Detection Technologies*, pp. 5–81, edited by M. Henini and M. Razeghi, Elsevier, Amsterdam, 2002.

16. A. Rogalski, "Quantum well photoconductors in infrared detector technology", *J. Appl. Phys.* **93**, 4355–4391 (2003).

17. A. Rogalski and W. Larkowski, "Comparison of photodiodes for the 3–5.5 μm and 8–12 μm spectral regions", *Electron Technology* **18**(3/4), 55–69 (1985).

18. J. Wenus, J. Rutkowski, and A. Rogalski, "Two-dimensional analysis of double-layer heterojunction HgCdTe photodiodes", *IEEE Trans. Electron Devices* **48**, 1326–1332 (2001).

19. P. Capper, T. Tung, and L. Colombo, "Liquid phase epitaxy" in *Narrow-Gap II-VI Compounds for Optoelectronic and Electromagnetic Applications*, pp. 30–70, edited by P. Capper, Chapman@Hall, London, 1997.

20. Y. Nemirowsky, S. Margalit, E. Finkman, Y. Shacham-Diamand, and T. Kidron, "Growth and properties of Hg$_{1-x}$Cd$_x$Te epitaxial layers", *J. Electronic Materials* **11**, pp.133–153, 1982.

21. J.S. Chen, Y.L. Wu, C.D. Chiang, and T.B. Wu, "Growth of Hg$_{1-x}$Cd$_x$Te heterolayers by slider LPE using separate compensating atmosphere of mercury", *J. Crystal Growth* **113**, 520–526, 1991.

22. T.Tung, L.V. DeArmond, R.F. Herald, P.E. Herning, M.H. Kalisher, D.A. Olson, R.F. Risser, A.P. Stevens, and S.J. Tighe, "State of the art of Hg-melt LPE HgCdTe at Santa Barbara Research Center", *Proc. SPIE* **1735**, 109–131 (1992).

23. J. Piotrowski and M. Razeghi, "Improved performance of IR photodetectors with 3D gap engineering", *Proc. SPIE* **2397**, 180–192 (1995).

24. J. Piotrowski, M. Grudzień, Z. Nowak, Z. Orman, J. Pawluczyk, M. Romanis, and W. Gawron, "Uncooled pho-

tovoltaic Hg$_{1-x}$Cd$_x$Te LWIR detectors", *Proc. SPIE* **4130**, 175–184 (2000).

25. J. Piotrowski and A. Rogalski, "New generation of infrared photodetectors", *Sensors and Actuators* **A67**, 146–152 (1998).

26. J. Piotrowski, "(1–15)-μm Cd$_x$Hg$_{1-x}$Te photodiodes with protected junction surface", *Biuletyn. WAT*, No. 9, 93–100 (1976). (in Polish).

27. C. Musca, J. Antoszewski, J. Dell, L. Faraone J. Piotrowski, and Z. Nowak, "Multi-junction HgCdTe long wavelength infrared photovoltaic detector for operation at near room temperature", *J. Electronic Mat.* **27**, 740–746 (1998).

28. W. Gawron, K. Adamiec, K. Jóźwikowski, and A. Rogalski, "High sensitivity 8–14-μm HgCdTe photodetectors operated at ambient temperature", *Proc. SPIE* **3948**, 94–103 (2000).

29. W. Gawron and A. Rogalski, "HgCdTe buried multi-junction photodiodes fabricated by the liquid phase epitaxy", *Infared Physics and Technol.* **43**, 157–163 (2002).

30. H.K. Gummel, "A self-consistent iterative scheme for one-dimensional steady state transistor calculations", *IEEE Trans. Electron Devices* **ED 11**, 455–465 (1964).

31. A. De Mari, "An accurate numerical steady-state one-dimensional solution of the p–n junction", *Solid State Electronics* **11**, 33–58 (1968).

32. D.L. Scharfetter and H.K. Gummel, "Large-signal analysis of a silicon read diode oscillator", *IEEE Trans. Electron Devices* **ED 16**, 64–77 (1969).

33. M. Kurata, *Numerical Analysis of Semiconductor Devices,* Lexington Books, DC Heath (1982).

34. W.L. Engl, H.K. Dirks, and B. Meinerzhagen, "Device modeling", *Proc. IEEE* **71**, 10–33 (1983).

35. Computer programme *Semicad Devices*, Dawn Technologies Inc., California, 1994.

36. Computer programme *Apsys*, Crosslight Software Inc., Ontario, 1998.

37. W. Van Roosbroeck, "Theory of the electrons and holes in germanium and other semiconductors", *Bell Syst. Tech. J.* **29**, 560–607 (1950).

38. K. Jóźwikowski, "Numerical modelling of fluctuation phenomena in semiconductor devices", *J. Appl. Phys.* **90**, 1318–1327 (2001).

39. K. Jóźwikowski and A. Rogalski, "Computer modelling of dual-band HgCdTe photovoltaic detectors", *J. Appl. Phys.* **90**, 1286–1291 (2001).

40. K. Jóźwikowski, A. Rogalski, and A. Jóźwikowska, "Numerical modelling of fluctuation phenomena in semiconductors and detailed noise study of mid-wave infrared HgCdTe-heterostructure devices", *J. Electron. Mater.* **31**, 677–682 (2002).

41. M. B. Reine, A. Hairston, P. O'Dette, S. P. Tobin, F. T. J. Smith, B. L. Musicant, P. Mitra, F. C. Case, "Simultaneous MW/LW dual-band MOCVD HgCdTe 64×64 FPAs", *Proc. SPIE* **3379**, 200–212 (1998).

42. C.T. Elliott, N.T. Gordon, R.S. Hall, T.J. Phillips, C.L. Jones, and A. Best, "1/f noise studies in uncooled narrow gap Hg$_{1-x}$Cd$_x$Te non-equilibrium diodes", *J. Electronic Materials* **26**, 643–648 (1997).

43. G.S. Kousik, C.M. van Vliet, G. Bosman, and P.H. Handel, *Adv. Phys.* **34**, 663 (1985).